Heller, Valentin (2015) Composite modelling of the effect of the water body geometry on landslide-tsunamis. In: 36th IAHR World Congress, 28 Jun - 03 Jul 2015, Delft, the Netherlands.

Composite modelling of the effect of the water body geometry on landslide-tsunamis

Conference Paper · July 2015

1 author:

Valentin Heller
University of Nottingham
43 PUBLICATIONS **375** CITATIONS

E-proceedings of the 36th IAHR World Congress
28 June – 3 July, 2015, The Hague, the Netherlands

COMPOSITE MODELLING OF THE EFFECT OF THE WATER BODY GEOMETRY ON LANDSLIDE-TSUNAMIS

VALENTIN HELLER

Fluid and Particle Processes Research Group, Faculty of Engineering, University of Nottingham, Nottingham, UK, Valentin.heller@nottingham.ac.uk

ABSTRACT

Subaerial landslide-tsunamis (impulse waves) are generated by mass movements such as landslides, rock falls or glacier calving interacting with a water body. Preliminary landslide-tsunami hazard assessment is commonly based on empirical equations derived from wave channel (2D) or wave basin (3D) experiments. It is crucial to select the most appropriate set of empirical equations for a particular case as the difference in the far-field wave height between 2D and 3D may exceed an order of magnitude. The present study systematically investigates the effect of the water body geometry on the wave characteristics. Physical model tests were conducted in 2D and repeated in 3D, involving two water depths, three rigid slides and different subaerial slide release positions. The waves were found to decay in 2D considerably slower with distance $x^{-0.30}$ than in 3D with radial distance $r^{-1.0}$. The 3D wave heights in the slide impact zone can be identical large as in 2D for a large slide Froude number F, relative slide thickness S and relative mass M. However, for small F, S and M, the 3D waves are considerably smaller, both in the near- and far-field. Empirical equations are presented to transform wave parameters from 2D to 3D. One 2D-3D test pair, involving a solitary-like wave, is investigated in detail regarding the slide kinematics, water surface elevations and slide-water interaction power. This power is derived from pressure measurements on the slide front and the slide kinematics. The identical test pair is then used to calibrate the Smoothed Particle Hydrodynamics SPH code DualSPHysics and to numerically investigate the wave features in five intermediate geometries between 2D and 3D. For a "channel" geometry with diverging side wall angle of 7.5°, the wave amplitudes along the slide axis were found to lie approximately halfway between the values observed in 2D and 3D. At 45°, the values are practically identical to those in 3D. These findings support preliminary landslide-tsunami hazard assessment.

Keywords: Composite modelling; Impulse wave; Landslide-tsunami; Physical modelling; Smoothed Particle Hydrodynamics

1. INTRODUCTION

Landslide-tsunamis (impulse waves) are caused by mass movements such as landslides, rockfalls, snow avalanches, ice calving or asteroids interacting with a water body. Such waves are commonly referred to as tsunamis in an ocean and as impulse waves in more restricted water bodies such as fjords, lakes or reservoirs. Extreme examples include the 1958 Lituya Bay case with a run-up height of 524 m (Miller, 1960) and the 1963 Vajont case where an impulse wave overtopped a dam by approximately 70 m resulting in around 2,000 casualties (Müller, 1964).

Such waves are mainly mitigated with passive methods including early warning, evacuation, reinforced infrastructure, safety clearance from ice calving prone areas, reservoir drawdown or provision of adequate freeboard of dam reservoirs. These methods require detailed knowledge about the tsunami features and a common method to estimate these features are generic empirical equations (Heller et al., 2009). Such equations express the unknown wave parameters as a function of the slide impact characteristics (slide properties, hill slope angle, water depth) and the wave propagation parameters (distance from the source, propagation direction).

A short-coming of generic empirical equations is that they are commonly based on the idealised water body geometries wave channel (2D, e.g. Heller and Hager, 2010) or wave basin (3D, e.g. Huber and Hager, 1997). Both geometries have their justification in real-world applications, and may be considered as two extreme cases of naturally occurring geometries (Heller et al., 2009):

(i) 2D (line source): The slide impacts longitudinally, the slide width b_s being identical or larger than the water body width b. The waves are confined as they move along x, the longitudinal direction of the water body without transverse or radial spreading.

(ii) 3D (point source): The slide, with a width $b_s < b$, impacts into a larger water body. The waves propagate laterally and radially from the slide impact zone and can be described in cylindrical coordinates with the radial distance r and the wave propagation angle γ.

The physical understanding of the effect of the water body geometry on landslide-tsunamis and impulse waves is relatively limited. The most significant contribution to this field (Chang et al., 1979; Heller et al., 2009; 2012; Huber and Hager, 1997; Jiang and LeBlond, 1994; Kranzer and Keller, 1959; Watts et al., 2005) were reviewed by Heller and Spinneken (2015). The present article aims to investigate the effect of the water body geometry on landslide-tsunamis with a composite (experimental-numerical) modelling approach and to enhance our physical understanding of the slide-water interaction power based on novel, high quality measurements.

2. PHYSICAL MODEL

The 2D experiments were conducted in the Coastal Wave Flume and the 3D tests in the Wave Basin, both located in the Hydrodynamics Laboratory of the Department of Civil and Environmental Engineering at Imperial College London. The set-ups are described in detail in Heller and Spinneken (2015) and Heller et al. (2015). The plan area unobstructed by any beach or wavemaking system was 21.0 m × 0.6 m for the flume and 7.4 m × 20.0 m for the basin.

The hill slope ramp shown in Figure 1, previously used by Heller and Spinneken (2013), was re-used, where the slope angle was $\alpha = 45°$ for all tests. The ramp covered the entire channel width (2D), while its sides were extended by up to 7.75 m long walls in 3D (Figure 2). These walls were inclined at an angle of $\alpha = 45°$ corresponding to the exact ramp inclination. The front surface of the ramp consisted of PVC sheets. A stainless steel plate and a circular-shaped transition made of stainless steel were placed at the ramp toe in both 2D and 3D (Figure 2(a)). The transition was bent to an eighth of a circle of radius 0.60 m (Figure 1).

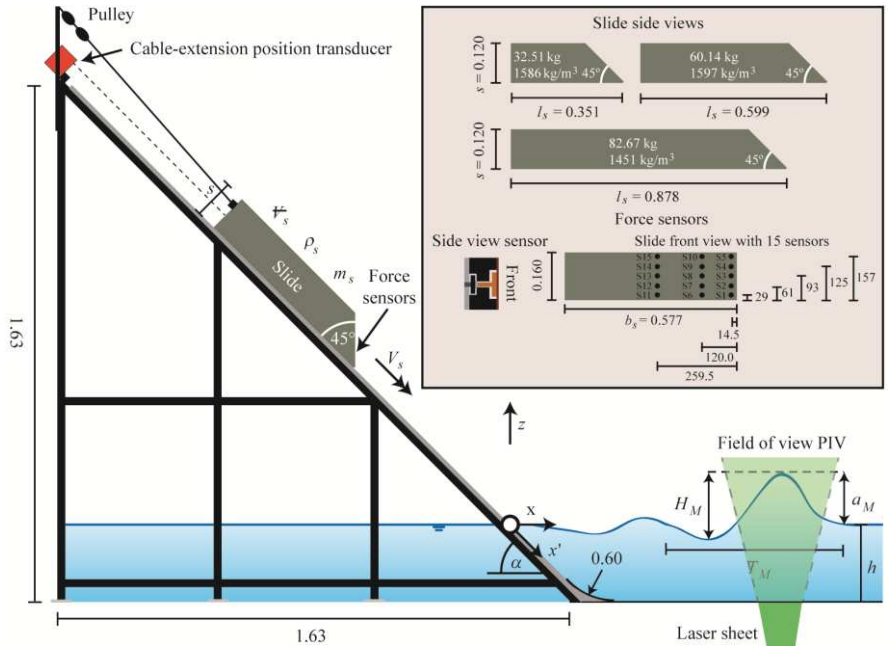

Figure 1. Side view of set-up and measurement systems including slide properties and force sensor locations show in the grey box; all length dimensions are in m except for the force sensor locations which are given in mm.

The tsunamis were generated with three rigid slides made of PVC, with the properties shown in the grey box in Figure 1. The slide top surfaces were essentially flat as all components and electrical cables were integrated into the slides. The two longer slides were built of the shortest slide and rear extensions such that the front face, including a number of force sensors embedded therein, was identical in all cases. The slide masses were m_s = 32.51, 60.14 and 82.67 kg and the corresponding densities ρ_s = 1586, 1597 and 1451 kg/m^3. The slide widths b_s = 0.577 m and thicknesses s = 0.120 m were constant while the three lengths were l_s = 0.351, 0.599 and 0.878 m (Figure 1).

Figure 1 shows additional slide parameters namely the slide volume $\forall_s$ and the slide centroid impact velocity V_s. Also shown are the hill slope angle $\alpha = 45°$ and still water depth h. The evolution of the wave parameters depends on the horizontal distance x in 2D, whereas the radial distance r and the wave propagation angle γ are adopted in 3D. In both cases, the coordinate origin is placed at the intersection of the slide axis with the water surface and the hill slope face. The origin for the coordinate along the hill slope x' is placed at the identical location. The most relevant unknown wave parameters are the maximum wave amplitude a_M, height H_M and period T_M.

The test programme is shown in Table 1 and includes 18 main tests conducted in both 2D and 3D. The dimensional parameters were varied in wide ranges and all four wave types Stokes-, cnoidal-, solitary- and bore-like waves were investigated (Heller and Hager, 2011). The test programme included three slides and two water depths h = 0.240 and 0.480 m. Each slide was released from three different release positions x', resulting in three slide impact velocities $0.94 \le V_s \le 3.79$ m/s. The slide nose was located at $x' = 0$ prior to release for the lowest V_s values. The dimensionless parameters include the slide Froude number $0.54 \le F = V_s/(gh)^{1/2} \le 2.47$ with gravitational acceleration g, relative slide thickness $0.25 \le S = s/h \le 0.50$, relative slide mass $0.25 \le M = m_s/(\rho_w b_s h^2) \le 2.49$ with water density ρ_w, and hill slope angle $\alpha = 45°$. The effect of the water body geometry may also depend on the slide width to length ratio $0.66 \le b_s/l_s \le 1.64$ (Jiang and LeBlond, 1994). However, since b_s is already included in M, and l_s is expressed as $l_s \approx \forall_s/(sb_s)$ for the present block model study, the parameter b_s/l_s is not independent and already considered by S and M (Heller and Spinneken, 2015).

The measurement systems include (i) a cable-extension position transducer to measure the slide kinematics in 2D and 3D, (ii) 15 force sensors integrated into the slide front to measure pressures during slide impact in 2D, (iii) resistance type wave gauges to measure the wave properties (2D and 3D), (iv) Particle Image Velocimetry PIV to measure the slide kinematics at different positions along the flume (2D) and (v) a video camera for visual observations. The present study presents results from (i), (ii), (iii) and (v). Details about these measurement systems are available from Heller and Spinneken (2015) and Heller et al. (2015) and the locations of the force sensors are given in Figure 1.

The wave features were recorded at 128 Hz using wave probes located at relative distances $x/h = r/h = 3.0$, 5.0, 7.5, 10.0, 15.0, 22.5 and 35.0 (2D and 3D), with exception of $r/h = 35$ for $h = 0.480$ m in 3D and some onshore waves in 3D ($\gamma = 90°$). The wave propagation angles in 3D are $\gamma = 0$, 15, 30, 45, 58, 73 and 90° (onshore wave run-up). The onshore wave run-up probes consisted of stainless steel strips bonded to the surface of the side walls (Figure 2(a)).

Table 1. Test programme with dimensional and dimensionless parameters in 2D; all slide parameters are identical in 3D except for the slide velocity which may vary by up to ±5%; the numbers in bold are for the test pair presented in Figures 2, 4, 5, 6 and 9.

Slide type	h (m)	V_s (m/s)	s (m)	m_s (kg)	b_s (m)	F (-)	S (-)	M (-)
Short slide	0.240	0.94, 2.54, 3.79	0.120	32.51	0.577	0.61, 1.66, 2.47	0.50	0.98
	0.480	1.16, 2.38, 3.12	0.120	32.51	0.577	0.54, 1.10, 1.44	0.25	0.25
Medium slide	**0.240**	1.21, **2.32**, 3.14	**0.120**	**60.14**	**0.577**	0.79, **1.51**, 2.05	**0.50**	**1.81**
	0.480	1.47, 2.45, 3.21	0.120	60.14	0.577	0.68, 1.13, 1.48	0.25	0.45
Long slide	0.240	1.37, 2.17, 2.78	0.120	82.67	0.577	0.89, 1.42, 1.81	0.50	2.49
	0.480	1.89, 2.53, 3.01	0.120	82.67	0.577	0.87, 1.17, 1.39	0.25	0.62

Figure 2. Physical model test in 3D with (a) initial conditions and (b) tsunami generation and propagation at $t \approx 0.7$ s.

3. NUMERICAL MODEL

3.1 Overview

Smoothed Particle Hydrodynamics SPH was used for the numerical simulations of one 2D-3D test pair. Details about SPH are available from reviews such as Crespo et al. (2013), Gómez-Gesteira et al. (2010), Liu and Liu (2003) and Monaghan (1992). SPH is a Langrangian mesh-less method in which the fluid is represented by nodal points. Each nodal point represents a fluid particle with physical quantities (mass, density, velocity, pressure) and interacts with neighbouring particles according to the Navier-Stokes equations. The values of the aforementioned quantities at a particular point are found by interpolation over the neighbouring particles (Gómez-Gesteira et al., 2010).

The SPH open source code DualSPHysics with the beta executable of v3.1 was used herein (Crespo et al., 2013) with the Verlet time integration scheme, cubic spline kernel function, Delta-SPH density filter, artificial viscosity and dynamic boundary conditions. The beta executable v3.1 includes a Discrete Element Method DEM formulation such that solid-solid and solid-fluid interactions can be simulated where the inter-particle forces of rigid body particles are derived from contact law theories. The DEM particles are regarded by the fluid particles as SPH particles, allowing for a natural coupling between SPH and DEM (Canelas et al., 2013). These features are essential for the present work, as the slide is modelled as a floating object moving along a rigid-ramp boundary.

Integrated post-processing tools within DualSPHysics were used both to visualise the results and to extract the free surface data at a set of points. The free surface is visualised as a mass isosurface at a relative mass value of 0.5, and the floating objects are represented as polygons that track the underlying particles. All simulations were performed on the Imperial College London HPC CX1 clusters with 12 CPUs. Figure 3 shows the seven numerical domains of the presented test pair including a side view and a plan view of the 2D geometry (Figure 3a,b) and plan views of the remaining six geometries (Figure 3c-h). The overall domain length from the rear of the ramp to the end of the water body is 4.96 m in all cases. The ramp is 0.90 m long such that the pure water body length is 4.30 m (4.96 – ramp length + h) corresponding to $x = 7.5h + 2.50$ m. As a result, reflections are avoided for the primary wave at $x/h = 7.5$. The overall 3D domain is 6.45 m wide. The initial distance between particles was 10 mm. The shortest presented simulation (2D, numerically treated as a three-dimensional problem, $h = 0.240$ m, 10 mm initial distance between particles) took 70 minutes per second of real time and involved 1,008,227 particles. The computationally most expensive simulation presented (3D, $h = 0.240$ m, 10 mm) took 12.7 hours per second of real time and included 8,239,107 particles. The initial distance between particles of 10 mm provides a good compromise between simulation time and accuracy.

3.2 Calibration and validation of DualSPHysics

The numerical model tests were calibrated with the physical model tests conducted in 2D and validated with the 3D tests. In the interest of computational time, the slide starts with the nose at the water surface with a prescribed initial slide front impact velocity V_{sf}. In initial tests, the velocities V_{sf} were identical to the measured values in the physical model tests. However, this resulted in numerical generated wave amplitudes in excess of the physical model tests. To enable a direct

comparison between the numerical and physical tests, the initial numerical slide velocity was reduced until a reasonable agreement in terms of wave amplitudes was achieved. It is important to stress that the velocity V_{sf} was the only parameter which was different between the numerical and the physical model tests and all slide features, the slope transition as well as the water body geometries being kept entirely consistent.

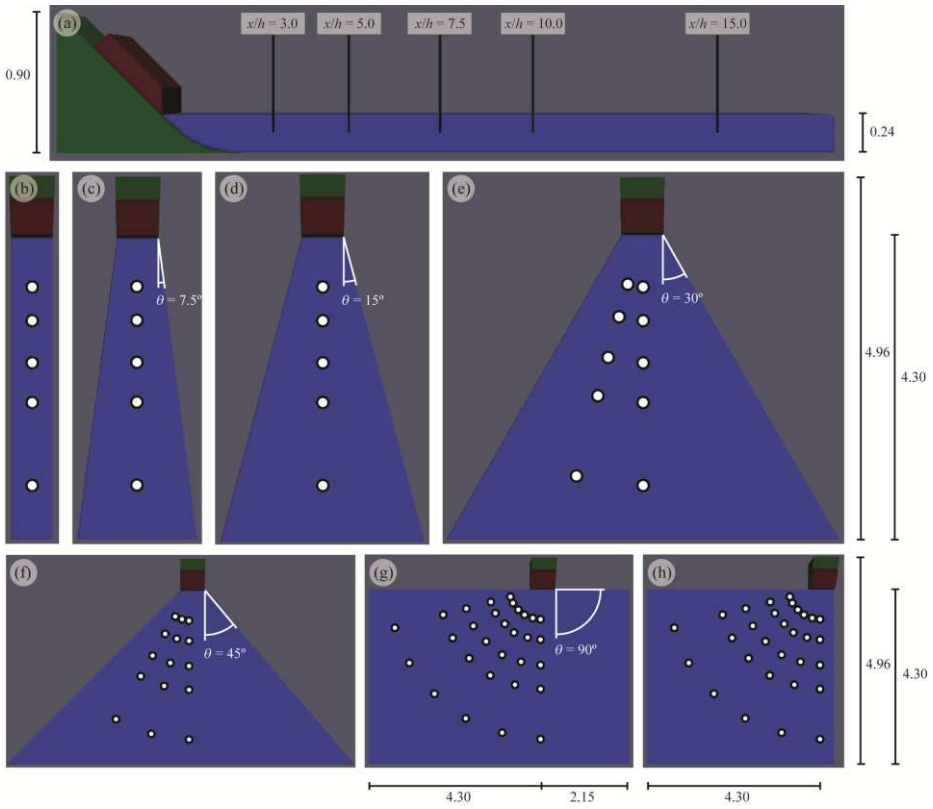

Figure 3. Initial configurations in DualSPHysics of the seven investigated water body geometries with wave probe locations: (a) side view and (b) plan view of 2D case (channel side wall angle $\theta = 0º$), (c) 7.5º, (d) 15º, (e) 30º, (f) 45º, (g) 3D case ($\theta = 90º$) and (h) 3D corner case (3Dc).

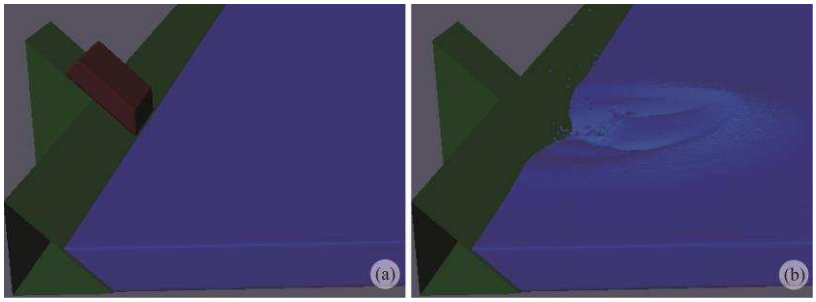

Figure 4. 3D numerical model test with (a) initial condition and (b) tsunami generation and propagation at $t \approx 0.7$ s (as in Figure 2).

Figure 4 shows the numerical simulation of the test corresponding to the experimental observations in Figure 2. The slide is released in Figure 4(a) from its initial position with a prescribed initial velocity. It then impacts into the 3D water body in Figure 4(b) and generates a splash which is considerably smaller than in the physical model test (Figure 2(b)). This marked difference is due to the initial distance between particles of 10 mm, for which the water sheet or individual droplets cannot adequately be simulated. Despite of these differences, the important features, namely the overall shape of the primary wave including its propagation on a semi-circle and the spatial variation in amplitude from the main impulse direction ($\gamma = 0$) towards the peripheries, are simulated qualitatively correctly.

4. RESULTS AND DISCUSSION

4.1 Slide kinematics and slide-water interaction power

Figure 5(a) shows the slide positions of the highlighted test pair in Table 1, in 2D (black lines) and 3D (grey lines). At time $t = 0$ the slide nose reaches the still water surface ($x' = 0$). The position measurement follows x' as long as the slide moves parallel to the ramp, i.e. until the slide nose reaches the transition. For any subsequent times, the actually measured distance between the slide rear and the position sensor deviate from the x' coordinate. The 3D tests were repeated under variations of the slide release position until the slide centroid impact velocity $V_{s,3D} = V_{s,2D} \pm 5\%$ for each test pair. As a result, the slide release positions in 2D and 3D differ slightly in Figure 5(a) with $x' = -0.55$ m (2D) and -0.47 m (3D).

Slides in 3D tend to run-out farther than in 2D. This is likely to be due to a small sub-pressure occurring below the slide when it passes over the transition. This is a direct consequence of the slide lengths, which are sufficiently long such that the slides are only supported at two contact points over the transition. This sub-pressure effect is believed to be larger in 2D, with limited lateral water supply when compared to 3D. The radius of the transition (0.60 m) was selected relatively large in order to limit this sub-pressure effect. Fortunately, if physical and numerical model results are considered individually, this effect is only expected to have a minor influence on the present results, as the main wave generation process is already concluded once the slide reaches the transition. However, this effect may be important if physical and numerical results are compared with one another, as the numerical model is currently not able to consider this effect (Heller et al., 2015).

Figure 5(a) also includes the slide velocities, which were directly derived from the positions through numerical discretisation. The slide reaches its peak velocity shortly after its nose reaches the still water surface. The slide centroid impact velocities $V_s \approx 2.32$ m/s, marked with arrows in Figure 5(a), are smaller than the peak velocities. In context of the numerical simulations, particular attention must be paid to the slide front impact velocity V_{sf}. The velocity V_{sf} is similarly in magnitude to the slide centroid impact velocity V_s in the presented case. The dashed lines in Figure 5(a) show the numerical slide positions and velocities. The numerical slide starts with a reduced slide front impact velocity in order to match the wave amplitudes of the physical model tests (Section 4.3). The numerical slide velocity adjusts then to the physical slide velocity. The main reason for this difference may again be the sub-pressure below the slide, which can currently not be represented in DualSPHysics. Also the friction between the slide and ramp surface is challenging to model.

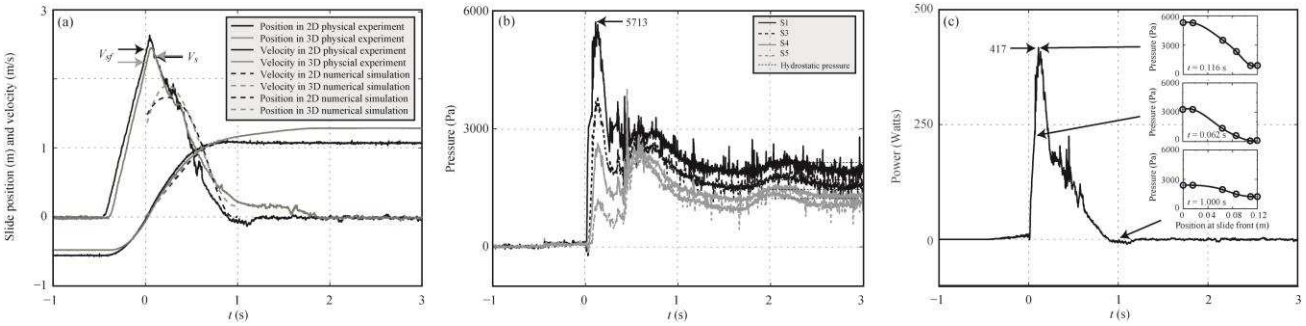

Figure 5. Slide impact features of the highlighted test pair in Table 1 versus time with $t = 0$ when the slide nose reaches the still water surface: (a) measured and simulated positions and velocities, (b) pressure on slide front in 2D measured with S1, S3, S4 and S5 (Figure 1) and (c) slide-water interaction power based on measurements with inserts showing pressure distributions over the slide front.

4.2 Pressure and slide-water interaction power in 2D

The analysis of the pressure data showed that the pressure distribution is uniform across the slide width, and boundary or side gap effects are insignificant up to 14.5 mm from the slide edge (Figure 1). Figure 5(b) shows the measured pressures in one section involving sensors S1, S3, S4 and S5 versus time. The pressure at S1, most adjacent to the slide nose, increases first, followed by similarly shaped signals measured by S3, S4 and S5. The peak pressure at S1 is 5713 Pa and this value is 2.4 times larger than the hydrostatic still water pressure at the channel bottom ($\rho_w g h = 2353$ Pa). This peak's maximum may mainly be dominated by the slide front impact velocity V_{sf} (Heller et al., 2015). The pressure signals of the remaining sensors S3, S4 and S5 are delayed compared to S1 and of considerably smaller magnitude, e.g. the pressure peak at S5 at the corresponding time as for sensor S1 is approximately 4.5 times smaller. The magnitude of the initial peak at S5 is exceeded once the slide reaches the channel bottom at $t > 1$ s. Figure 5(b) also includes the hydrostatic pressure (dashed lines) derived for the height of each individual force sensor when the slide sits flat on the channel bottom. The observed differences are expected, as the free water surface is unsteady and the sensors measure a combination of static and dynamic pressure components.

Figure 5(c) includes the instantaneous slide-water interaction power $P(t)$ deduced at the slide front surface. As the slide front is the main interface transferring energy to the water body, $P(t)$ may give a good indication when and how much slide energy is transferred into wave energy. The power was computed through $P(t) = F(t)V(t)\cos\alpha$, where the instantaneous force $F(t)$ on the slide front was computed from the spatial integration of the pressure signals in Figure 5(b). For this integration, the unknown boundary values were approximated with the values from S1 (nose) and S5 (top) and the resulting six points were interpolated using a cubic spline over the slide front as shown for three selected moments in time with the insets in Figure 5(c). The pressure magnitudes in these distributions increase with time starting from the slide nose, reach their maxima at the power peak and result then in a nearly linear distribution at $t = 1.0$ s, when the slide already reached the channel bottom in this particular case. These pressure curves, integrated over the slide height and multiplied by the slide width, resulted in $F(t)$. The instantaneous velocity $V(t)$ is available from Figure 5(a).

Figure 5(c) shows that the major power peak of 417 Watts occurs at approximately 0.2 s, and that nearly all energy is transferred within 0.5 s. Video recordings confirm that this closely relates to the time interval in which an impact crater forms and where the most important tsunami generation phase takes place. For such fast impacting slides with $V_{sf} = 2.43$ m/s, the front face is mostly responsible for the tsunami generation process. This explains why the relative volume M typically only has a secondary effect on the wave magnitude; the primary drivers being the slide Froude number F and the relative slide thickness S.

4.3 Wave profiles

Figure 6(a-d) shows the relative water surface elevations η/h of the 2D test from Figure 5. The abscissa shows the relative time $t(g/h)^{1/2}$, and the water surface elevations are shown for different wave probe locations along the slide axis (γ = 0). It is obvious that the wave type in 2D is solitary-like (Heller and Hager, 2011). Figure 6(e-h) includes the corresponding data of the 3D test, with the associated still images being shown in Figures 2 and 4. Note that the scale on the ordinate in the 3D case is increased by a factor of 2, 3 and 9 in Figure 6(f,g,h), respectively. The 2D relative primary wave amplitude at the first wave probe is a_{2D}/h = 0.189/0.240 = 0.79 and the corresponding 3D amplitude is only approximately 30% smaller with a_{3D}/h = 0.136/0.240 = 0.57. However, the 3D wave decays considerably faster than the 2D wave. In Figure 6(d,h) the primary wave amplitudes reduce to a_{2D}/h = 0.156/0.240 = 0.65 and a_{3D}/h = 0.010/0.240 = 0.04, respectively, resulting in a difference of a factor of 16. Figure 6 clearly illustrates the relevance of the effect of the water body geometry, and the associated need to investigate intermediate geometries.

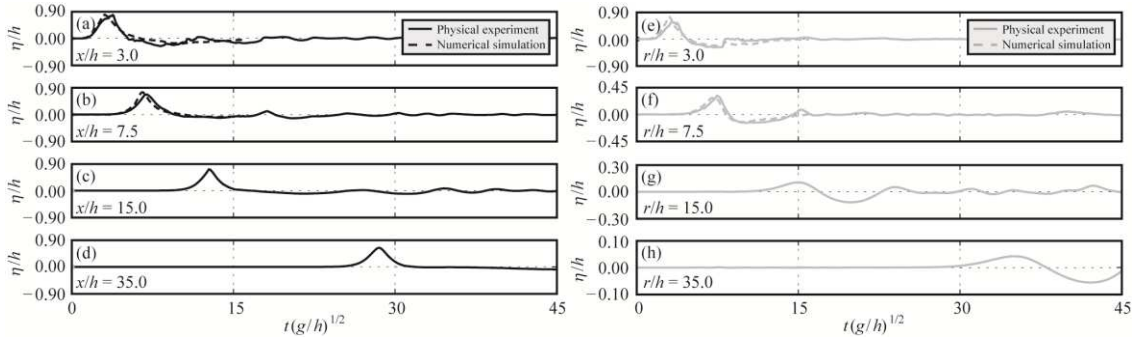

Figure 6. Comparison of relative water surface elevation η/h versus relative time $t(g/h)^{1/2}$ along the slide axis θ = 0º for the highlighted test pair in Table 1; the elevations are show for both 2D and 3D at (a,e) $x/h = r/h$ = 3.0, (b,f) 7.5, (c,g) 15.0 and (d,h) 35.0; note the increased scale on the ordinate in (f), (g) and (h).

Figure 6(a,b) further includes the numerically deduced wave profiles, which are shorter due to the restricted numerical domain size. The deviations between experimental and numerical results are small and lie within 11% relative to the primary wave amplitude *a*. After this successful calibration in 2D, the identical tests and slide impact velocities are validated against the 3D tests (Figure 6(e,f)). In this 3D comparison, maximum deviations between the physical and numerical amplitudes *a* of the primary waves are +33% (Figure 7(e)). A better agreement is achieved in Figure 7(f) with –20%. Particularly challenging is the numerical prediction of the trough length and of the secondary wave.

4.4 Comparison of 2D and 3D wave parameters

The 2D to 3D comparison presented herein is based on the primary wave (subscript 1) along the slide axis as its entire wave length is free from significant reflections and it is propagating in initially still water. Figure 7(a) includes the wave height decay along the slide axis for three distinct wave types. The curves describing the data start from a level which may be defined as a function of the slide impact characteristics F, *S* and *M*. The decay $(r/h)^{-1.0}$ results in a good overall approximation of both the 3D data in Figure 7(a) and of all 18 tests (Heller and Spinneken, 2015). Figure 7(a) also includes the corresponding 2D tests with wave decay $H_{2D} \propto x^{-0.30}$. The different decay behaviour of 2D and 3D tests is apparent, with 3D tests tending to be smaller and decaying much faster with distance from the source. Figure 7(b) shows the relative wave height $H_{3D,1}/h$ versus γ and different relative radial distances r/h (symbols) for a test with F = 0.65, *S* = 0.50 and *M* = 0.98. A good description with the decay term $(r/h)^{-1.0}\cos^{2\{1+\exp[-0.2(r/h)]\}}(2\gamma/3)$ is achieved, particularly in the far-field for $r/h \geq 10.0$. This decay term was used in Heller and Spinneken (2015) to describe all 18 tests in 3D.

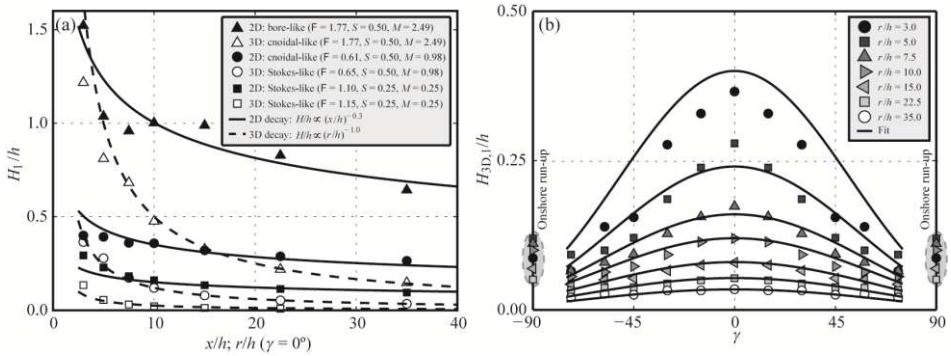

Figure 7. Primary wave height decay: (a) wave height evolution along the slide axis for three selected 2D-3D test pairs and (b) relative primary wave height decay $H_{3D,1}/h$ of a test with F = 0.65, *S* = 0.50 and *M* = 0.98 as a function of r/h and γ fitted with (-) $(r/h)^{-1.0}\cos^{2\{1+\exp[-0.2(r/h)]\}}(2\gamma/3)$; also included are the onshore wave run-up data at γ = 90º, which behave differently.

Figure 8 shows the spatial evolution of the primary wave parameters observed along the slide axis in 3D, relative to the parameters observed in 2D. This includes the primary amplitude ratios $a_{3D,1}(r/h, \gamma = 0°)/a_{2D,1}(x/h)$ in Figure 8(a) and the height ratios $H_{3D,1}(r/h, \gamma = 0°)/H_{2D,1}(x/h)$ in Figure 8(b). Different symbols refer to different slide Froude numbers F. The corresponding empirical equations are

$$a_{3D,1}(r/h,\ \gamma = 0º)/a_{2D,1}(x/h) = 1.9[(r/h)F^{-0.40}S^{-0.50}M^{-0.50}]^{-5/6} \quad (R^2 = 0.92) \quad [1]$$

$$H_{3D,1}(r/h,\ \gamma = 0º)/H_{2D,1}(x/h) = 1.8[(r/h)F^{-0.40}S^{-0.50}M^{-0.50}]^{-2/3} \quad (R^2 = 0.90) \quad [2]$$

The data in Figure 8 shows excellent data fit with the vast majority of data points lying within the ±50% bounds. The differences between 3D and 2D wave parameters vanish for large F, *S* and *M*. Figure 8 also shows conditions under which 3D waves may be as large as 2D waves in the slide impact zone. However, 3D and 2D wave heights differ for small F, *S* and *M* by up to a factor of 2.7 in the near-field (r/h = 3.0) and typically by an order of magnitude in the far-field. It is further interesting to observe that the wave amplitude ratios in Figure 8(a) are lower than the wave height ratios in Figure 8(b), namely 28% on average over all data. In other words, landslide-tsunamis in 3D show smaller wave amplitude to height ratios than in 2D. The 3D wave profile is not only smaller but also less non-linear than in 2D.

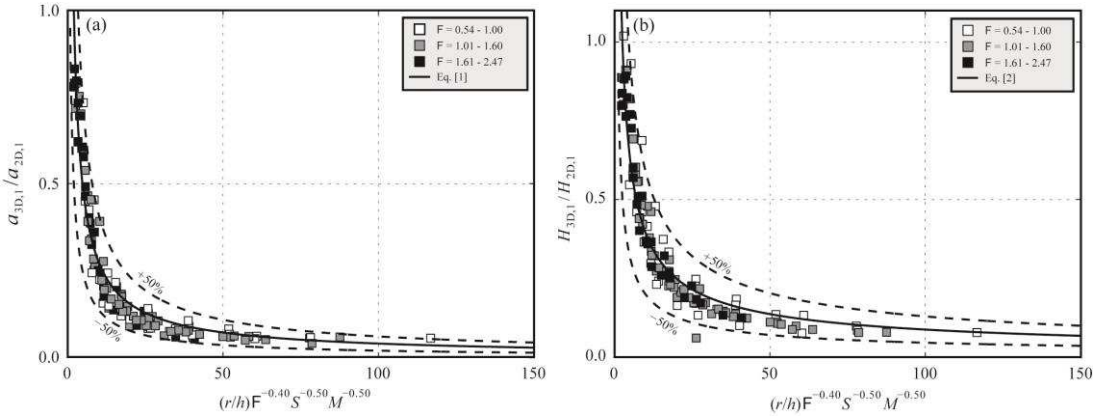

Figure 8. Ratios of 3D to 2D primary wave parameters along slide axis: (a) wave amplitude ratios $a_{3D,1}/a_{2D,1}$ with (-) Eq. [1] and (--) ±50% (R^2 = 0.92) and (b) wave height ratios $H_{3D,1}/H_{2D,1}$ with (-) Eq. [2] and (--) ±50% (R^2 = 0.90).

4.5 Numerically investigated intermediate geometries

This section addresses the wave parameters from five intermediate water body geometries between 2D and 3D, including the 3Dc case (Figure 3). Figure 9(a) shows the relative wave amplitude a/h along the slide axis for all seven geometries. The data are illustrated as a function of the relative distance x/h or r/h for the identical test as shown in Figures 2, 4, 5 and 6. The relative wave amplitudes for the various geometries at $x/h = r/h = 3.0$ are similar large and lie at $a/h = 0.73 \pm 10\%$. The wave amplitudes for a geometry with a channel side wall angle of $\theta = 7.5°$ lie approximately halfway between the values observed in 2D and 3D, and the 3D wave amplitudes are approached very rapidly with increasing θ. For $\theta = 30°$, the observed wave amplitudes are practically identical to those in 3D. As a result, the 3D case may be investigated in a geometry with $\theta = 30°$ for cases where only the maximum amplitude along the slide axis is of interest. This finding saves computational cost for numerical simulations, and laboratory space in a physical model study. The tsunami in the 3Dc geometry is clearly smaller than in 2D and its relative wave amplitudes a/h are close to the values for $\theta = 7.5°$. Figure 9(b) shows the relative wave heights H/h at the same locations and for the identical geometries as in Figure 9(a). Similar features as for the amplitude are observed, namely that the wave heights approach the values in 3D relatively rapidly with increasing θ, and that the values measured in 3Dc differ substantially from both 2D and 3D. Note that these findings apply for a test pair involving a solitary-like wave in 2D and not necessarily for other wave types (Heller et al., 2015).

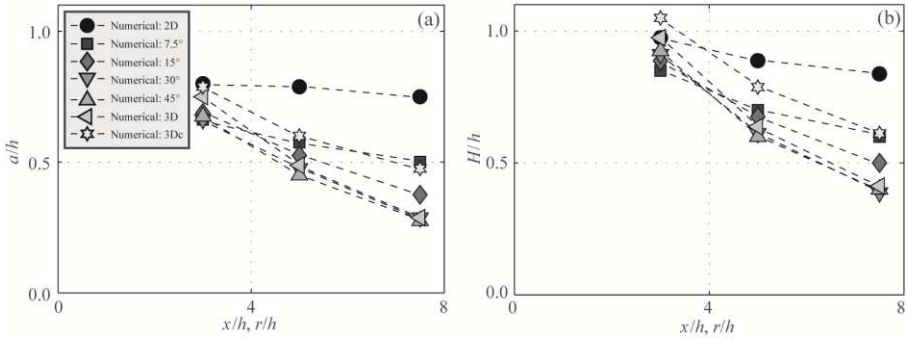

Figure 9. Numerical wave parameters along slide axis in seven different water body geometries: (a) relative wave amplitude a/h and (b) relative wave height H/h versus relative distance x/h and r/h, respectively.

5. CONCLUSIONS

Subaerial landslide-tsunamis were investigated adopting a composite (experimental-numerical) modelling approach. The primary aim of the work was to quantify the effect of the water body geometry to extend the application range of existing generic empirical equations used for preliminary landslide-tsunami hazard assessment. In total, 18 rigid slide tests were conducted in a wave channel (2D) and repeated in a wave basin (3D). A set of detailed measurements were obtained, including slide kinematics, fluid pressures and visual observations. These tests revealed that the waves decay in 2D

considerably slower with distance $x^{-0.30}$ than in 3D with radial distance $r^{-1.0}$. The 3D wave heights in the slide impact zone can be identical large as in 2D for a large slide Froude number F, relative slide thickness *S* and relative mass *M*. However, for small F, *S* and *M*, the 3D waves are considerably smaller, both in the near- and far-field. Empirical equations are presented to transform wave parameters from 2D to 3D.

One 2D-3D test pair, involving a solitary-like wave in 2D, was investigated in detail. The wave amplitude in this case was a factor of 16 larger in 2D than in 3D at $r/h = 35$. The slide kinematics combined with the measured pressures provided an instantaneous slide-water interaction power graph showing that the majority of the power is transferred within 0.5 s. This test pair was then used to calibrate the Smoothed Particle Hydrodynamics SPH open source code DualSPHysics v3.1, including a Discrete Element Method DEM to model the slide-ramp interaction. The numerical simulations were based on the same parameters as the physical model tests, except that the slide front impact velocity was reduced. The simulated wave amplitudes in 2D slightly over-estimated the experimentally observed amplitudes, by up to 11%, while the corresponding 3D numerical amplitudes deviate by up to +33%. The main reason for these discrepancies lay in the challenging slide kinematics. Five intermediate geometries between 2D and 3D were then addressed purely numerically including "channel" geometries with diverging side wall angles of $\theta = 7.5°$, 15°, 30° and 45° and the 3D corner case, with slide impact at the corner of a basin. For $\theta = 7.5°$, the wave amplitudes along the slide axes lay approximately halfway between the values observed in 2D and 3D, and the values are practically identical to those in 3D for $\theta = 30°$. These findings support hazard assessment as wave parameters from generic empirical equations derived in 2D and 3D can now be translated to additional geometries.

Many further experimental and numerical results of the effect of the water body geometry and physical insight into slide and wave kinematics as well as wave propagation (frequency dispersion) are presented in Heller and Spinneken (2015) and Heller et al. (2015). Future work aims to investigate the physical behaviour of landslide-tsunamis in more complex water body geometries involving larger domains and higher resolutions. Additional real-world predictions should also be examined to further investigate the potential of DualSPHysics in supporting hazard assessment. Recently announced improvements by the DualSPHysics developers strongly support these aims, including the implementation of the Riemann Solver and the improvement of the solid-solid interaction (slide kinematics), such that enhanced landslide-tsunami predictions may be expected in the near future.

ACKNOWLEDGMENTS

The support of Johannes Spinneken, Mark Bruggemann, the DualSPHysics developers and of students is acknowledged. This work was supported by the Natural Environment Research Council [Grant number NE/K000578/1]. The position of the author during this research project was funded by an Imperial College London Junior Research Fellowship. The numerical simulations were conducted on the HPC facilities of Imperial College London.

REFERENCES

Canelas R., Ferreira R.M.L., Crespo A.J.C., and Domínguez J.M. (2013). A generalized SPH-DEM discretization for the modelling of complex multiphasic free surface flows. 8th *International SPHERIC workshop*, Trondheim, Norway.

Chang P., Melville W.K., and Miles J.W. (1979). On the evolution of a solitary wave in a gradually varying channel. *J. Fluid Mech*. 95, 401-414.

Crespo A.J.C., Domínguez J.M., Gómez-Gesteira M., Barreiro A., Rogers B.D., Longshaw S., Canelas R., and Vacondio R. (2013). User guide for DualSPHysics code v3.0.

Gómez-Gesteira M., Rogers B.D., Dalrymple R.A., and Crespo A.J.C. (2010). State-of-the-art of classical SPH for free-surface flows. *J. Hydraul. Res*. 48 (supplement), 6-27.

Heller V., Bruggemann M., Spinneken J., and Rogers B.D. (2015). Composite modelling of subaerial landslide-tsunamis in different water body geometries and novel insight into slide and wave kinematics. *Coast. Eng.* (under review).

Heller V., and Hager W.H. (2010). Impulse product parameter in landslide generated impulse waves. *J. Waterw. Port C-ASCE* 136 (3), 145-155.

Heller V., and Hager W.H. (2011). Wave types of landslide generated impulse waves. *Ocean Eng*. 38 (4), 630-640.

Heller V., Hager W.H., and Minor H.-E. (2009). Landslide generated impulse waves in reservoirs - Basics and computation. *VAW-Mitteilung* 211, R. Boes (Ed.), ETH Zurich, Zurich.

Heller V., Moalemi M., Kinnear R.D., and Adams R.A. (2012). Geometrical effects on landslide-generated tsunamis. *J. Waterw. Port C-ASCE* 138 (4), 286-298.

Heller V., and Spinneken J. (2013). Improved landslide-tsunami predictions: effects of block model parameters and slide model. *J. Geophys. Res*., 118 (3), 1489-1507.

Heller V., and Spinneken J. (2015). On the effect of the water body geometry on landslide-tsunamis: physical insight from laboratory tests and 2D to 3D wave parameter transformation. *J. Geophys. Res*. (under review).

Huber A., and Hager W.H. (1997). Forecasting impulse waves in reservoirs. Proc., 19th *Congrès des Grands Barrages*, Florence, ICOLD, Paris, pp. 993-1005.

Jiang L., and LeBlond P.H. (1994). Three-dimensional modeling of tsunami generation due to a submarine mudslide. *J. Phys. Oceanogr*. 24 (3), 559-572.

Kranzer H.C., and Keller J.B. (1959). Water waves produced by explosions. *J. Appl. Phys*. 30 (3), 398-407.

Liu G.R., and Liu M.B. (2003). Smoothed Particle Hydrodynamics - a meshfree particle method. World Scientific, London.

Miller D.J. (1960). Giant waves in Lituya Bay, Alaska. *Geological Survey Professional Paper No*. 354-C, U.S. Government Printing Office, Washington, D.C.

Monaghan J.J. (1992). Smoothed Particle Hydrodynamics. *Ann. Rev. Astron. Astr*. 30, 543-574.

Müller L. (1964). The rock slide in the Vajont Valley. *Rock Mech. Eng. Geol*. 2 (3-4), 148-212.

Watts P., Grilli S.T., Tappin D.R., and Fryer G.J. (2005). Tsunami generation by submarine mass failure. II: predictive equations and case studies. *J. Waterw. Port C-ASCE* 131 (6), 298-310.